analytical chemistry

pubs.acs.org/ac Article

Advancing Tumor Microenvironment Analysis: A Fluorescence Nanosystem for Caspase-1 Monitoring and Synergistic Therapy

Chen Zhao, Mo Ma, Jukun Yang, Jingdan Sun, Ying Sun, Pinyi Ma,* Shan Jiao,* and Daqian Song*

Cite This: *Anal. Chem.* 2025, 97, 6240−6248

Read Online

ACCESS | Metrics & More | Article Recommendations | Supporting Information

ABSTRACT: The lack of precise, real-time analytical tools for monitoring tumor microenvironment changes during treatment hinders advancements in integrated diagnostic and therapeutic platforms. Traditional caspase-3 monitoring strategies are limited by their inability to address drug resistance and newly discovered apoptotic pathways, leading to reduced accuracy and practicality. To overcome these limitations, we developed a fluorescence-based "Trojan horse" nanosystem, PFpR@CM, featuring high-sensitivity Caspase-1 detection, tumor-targeted delivery, and photothermal therapy. Caspase-1 was selected as a biomarker due to its ability to provide accurate feedback on reactive oxygen species (ROS) generation. The system employs Fe-doped polydopamine nanoparticles and red fluorescent carbon quantum dots (RCQDs) as the analytical core, achieving a detection limit of 0.024 U/mL for Caspase-1 with a linear range of 0.05−1.0 U/mL. By integrating MG-63 cell membrane camouflage, PFpR@CM ensures tumor specificity and immune evasion, allowing precise in situ monitoring of ROS production during ferroptosis. Experimental results demonstrate that the system enables simultaneous real-time fluorescence tracking and localized therapeutic interventions, achieving over 80% tumor volume reduction in vivo with minimal systemic toxicity. This work establishes a novel analytical chemistry approach for multifunctional tumor monitoring and treatment, providing an innovative solution to challenges in precision oncology.

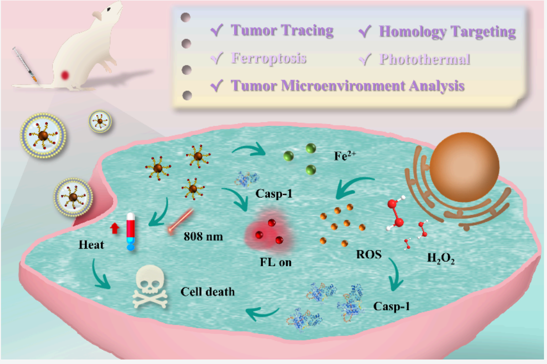

INTRODUCTION

The tumor microenvironment (TME) plays a pivotal role in the progression, metastasis, and treatment resistance of malignant tumors.[1,2] Comprising cancer cells, stromal cells, immune cells, and extracellular matrix components,[3,4] the TME is highly dynamic, characterized by hypoxia, acidosis, and changes in reactive oxygen species (ROS) levels.[5,6] Understanding and monitoring the TME is critical for advancing both diagnostics and therapeutics, as it directly influences tumor behavior and response to treatment.[7,8] Despite its significance, current tools for TME analysis are limited in their ability to provide precise, real-time insights into these dynamic changes during treatment.[9] This limitation hampers the development of integrated diagnostic and therapeutic platforms that can adapt to the evolving nature of tumors.

Traditional TME monitoring approaches, such as caspase-3-based apoptotic pathway analysis,[10,11] have shown limited accuracy due to their inability to capture the complexity of treatment-induced TME changes. These methods often fail to detect drug resistance promptly, reducing their practical applicability. To overcome these challenges, fluorescence-based analytical tools have emerged as promising solutions for real-time monitoring of TME biomarkers.[12] In particular, ROS-activated Caspase-1 has demonstrated significant potential as a biomarker.[13,14] Unlike caspase-3, Caspase-1 provides precise feedback on ROS levels, reflecting the oxidative stress-induced tumor cell death mechanisms critical in therapies like ferroptosis and photothermal therapy (PTT).[15−17]

Recent advancements in nanotechnology and biomimetic systems have opened new avenues for TME analysis.[18−20] Fluorescence nanosystems, such as those integrating red fluorescent carbon quantum dots (RCQDs), offer unique advantages in sensitivity and specificity for biomarker detection.[21−25] Furthermore, these systems can achieve multifunctionality by combining diagnostic and therapeutic capabilities. For instance, Fe^{2+}-doped polydopamine nanoparticles (PDA) enable efficient ROS generation via the Fenton reaction, which synergizes ferroptosis-based therapies with PTT. By incorporating biomimetic cell membrane camouflage, these nanosystems can enhance tumor-targeting specificity and evade immune clearance, addressing critical limitations of conventional approaches.[26−28]

In this study, we propose a novel "Trojan horse" nanodiagnostic integration platform that synergizes iron-

Received: January 7, 2025
Revised: March 4, 2025
Accepted: March 4, 2025
Published: March 11, 2025

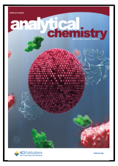

https://doi.org/10.1021/acs.analchem.5c00107

Scheme 1. Schematic Representation of Synthesis of PFpR@CM and Its Mechanism of Action. (A) Stepwise Synthesis of PFpR@CM. (B) Mechanism of Action of PFpR@CM in Cells

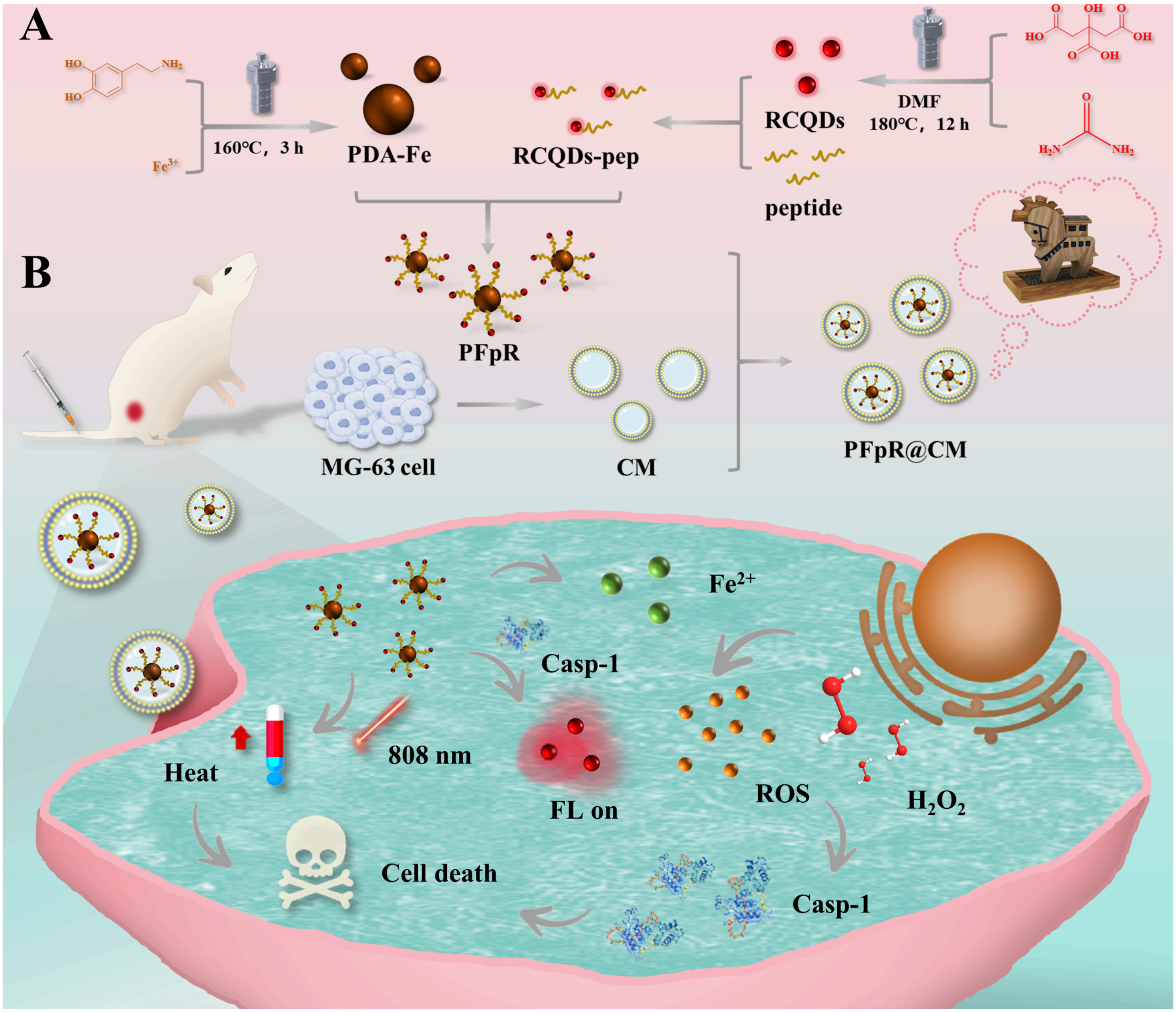

dependent cell death (ferroptosis) with PTT and is complemented with fluorescence imaging to track tumor location and treatment response. The fabrication involved doping Fe^{2+} ions into polydopamine (PDA) nanoparticles to form Fe-PDA (PF) complexes, followed by conjugation with a specific Caspase-1 substrate peptide (GRTYVADYTTL-PATC)[29] using a Michael addition reaction.[30] Red-emissive carbon quantum dots (RCQDs) were attached to the distal end of the peptide chain as a fluorescence reporter, creating the PFpR nanoparticle. However, as PFpR lacks intrinsic tumor-targeting capabilities and is recognized as a foreign substance, it is susceptible to rapid clearance by the immune system.[31] To circumvent this issue, we extracted membranes from MG-63 osteosarcoma cells and coated them onto PFpR nanoparticles to form a cell membrane-camouflaged PFpR@CM nanosystem, disguised as “Trojan horses” (Scheme 1A). Upon intravenous injection, PFpR@CM circulates through the bloodstream and accumulates at the tumor site via homotypic targeting enabled by the MG-63 cell membrane coating. Once internalized by tumor cells, the slightly acidic tumor microenvironment activates the Fe^{2+}-mediated Fenton reaction in the PDA core, which generates ROS.[32] This process activates Caspase-1, which then cleaves the peptide substrate, resulting in the release of RCQDs. As a result, the red fluorescence is restored, and the signaling pathway is activated, leading to tumor localization. Following fluorescence imaging, an 808 nm near-infrared laser was applied to the tumor site to initiate PTT to further enhance therapeutic efficacy through localized heating and tumor cell ablation (Scheme 1B).

EXPERIMENTAL PROCEDURE

Synthesis of RCQDs. RCQDs was synthesized using a hydrothermal method.[33] Thiourea (4.0 g) and citric acid (2.0 g) were dissolved in 20 mL of DMF. The resulting solution was heated in a Teflon-lined autoclave at 160 °C for 6 h. After cooling to room temperature, the reaction mixture was combined with 40 mL of NaOH solution (50 mg/mL) and stirred for 10 min. The mixture was then subjected to centrifugation at 13,000 rpm for 17 min, and the supernatant

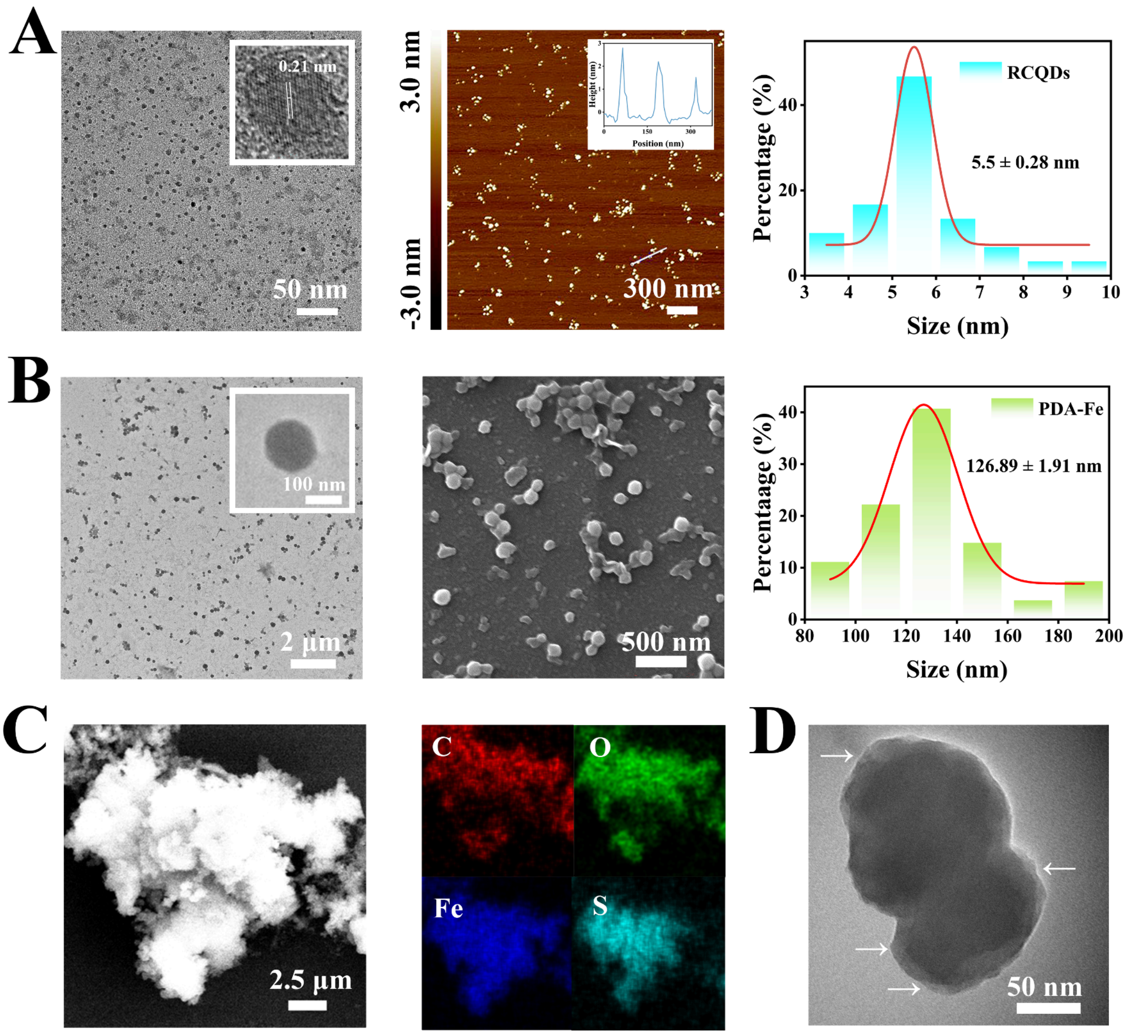

Figure 1. (A) TEM, HRTEM, and AFM images and particle size distribution of RCQDs. (B) TEM and SEM images and particle size distribution of PF. (C) EDC images of PFpR. (D) TEM image of PFpR@CM.

was collected. The supernatant was subsequently diluted with 50 mL of hydrochloric acid (HCl, 5%, v/v) and stirred for an additional 10 min. The solution was recentrifuged at 12,000 rpm for 15 min, and the resulting supernatant was collected and stored at 4 °C for subsequent use.

Synthesis of PDA-Fe (PF). The PF composite was synthesized by a hydrothermal method.[34] First, 11.4 mg of DOPA was dissolved in 30 mL of deionized water to obtain a DOPA solution with a pH of ~5. Then, 16.2 mg of $FeCl_3 \cdot 6H_2O$ was added to the DOPA solution to achieve a Fe/DOPA molar ratio of 1:1. Upon the addition of $FeCl_3 \cdot 6H_2O$, the solution immediately changed from colorless to dark green, and its pH dropped to 3.5. The solution was then transferred to a Teflon-lined autoclave and heated at 160 °C for 3 h. After the reaction was complete, the autoclave was cooled to room temperature. Impurities were removed by centrifugation at 12,000 rpm for 5 min, and the product was washed several times with deionized water. The final product was stored in a refrigerator at 4 °C. For comparison, PDA NPs were synthesized under the same conditions but without the addition of $FeCl_3 \cdot 6H_2O$.

Synthesis of PDA-Fe-pep-RCQDs (PFpR). The synthesis of PFpR was carried out using the Michael addition reaction.[35] To initiate the reaction, 1 mL of PF solution was mixed with 5 μL of peptide substrate solution (2 mg/mL, sequence: GRTYVADYTTLPATC) in 2 mL of Tris buffer (pH 8.0), and the mixture was stirred for 12 h. The mixture was then centrifuged at 10,000 rpm for 10 min, and the precipitate was redissolved in PBS to yield PDA-Fe-pep (PFp). Next, 1 mL of RCQDs was added to 2 mL of MES buffer (pH 6.0, 10 mM). To this solution, 200 μL of EDS (9.5 mg/mL) and 200 μL of NHS (5.0 mg/mL) were added, and the mixture was stirred for 1 h. Following this activation step, PFp was added to the solution and stirred for an additional 12 h to obtain the final PFpR product.

Synthesis of PDA-Fe-pep-RCQDs@CM (PFpR@CM). MG-63 cells were harvested by centrifugation at 3000 rpm for 5 min and then washed three times with PBS. The cells were subjected to five freeze−thaw cycles, alternating between −80 °C and room temperature, to disrupt the membrane. Afterward, the lysed cells were centrifuged at 5000 rpm for 3 min, and the resulting pellet was redissolved in PBS to obtain the cell membrane solution. For membrane coating, 100 μL of the MG-63 cell membrane solution was mixed with 0.5 mL of PFpR. The mixture was then sonicated in an ultrasonic cleaner at a power of 150 W and a frequency of 50 kHz for 15 min to yield the PFpR@CM composite.

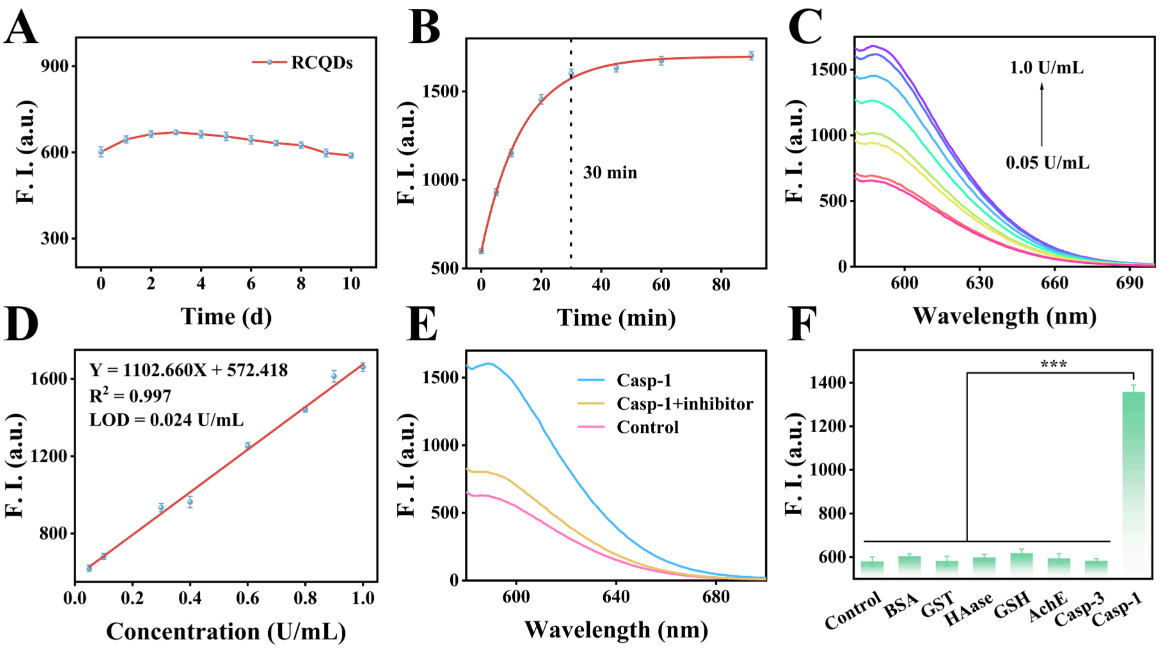

Figure 2. (A) Stability of fluorescence of RCQDs over time. (B) Time-dependent variation of FL intensity of PFpR@CM upon incubating with caspase-1 (1.0 U/mL) at 37 °C, pH 7.4. (C) FL intensity of PFpR@CM incubated with human caspase-1 at different concentrations (0.05, 0.1, 0.3, 0.4, 0.6, 0.8, 0.9, and 1.0 U/mL) at 37 °C, pH 7.4 for 30 min. (D) Linear response of PFpR@CM to caspase-1 at concentrations between 0.05 and 1.0 U/mL ($n = 3$). (E) Fluorescence intensity of PFpR@CM, PFpR@CM+caspase-1 and PFpR@CM+caspase-1+inhibitor. (F) Effect of common interfering substances on the fluorescence intensity of PFpR@CM. ($^*P < 0.05$, $^{**}P < 0.01$, and $^{***}P < 0.001$).

■ RESULTS AND DISCUSSION

Preparation and Characterization of PFpR@CM. Red fluorescence offers significant advantages in bioimaging due to its deeper tissue penetration capabilities.[36] CQDs are particularly suitable as fluorescent signal reporters owing to their excellent biocompatibility and photostability.[37] Leveraging these properties, we selected red fluorescent CQDs (RCQDs) as the fluorescent signal reporter motif. The physical appearance of RCQDs under bright and dark fields, along with their CIE chromaticity diagram and predicted structure are shown in Figure S1.

Transmission electron microscopic (TEM) images (Figure 1A) revealed that the synthesized RCQDs had an average particle size of approximately 5.5 nm, while high-resolution TEM (HTEM) images indicated a lattice spacing of 0.21 nm. The results from atomic force microscopy (AFM) further showed that the height of RCQDs was about 2 nm, and they were monodisperse and had uniform size distribution. TEM and scanning electron microscopic (SEM) images of PF nanoparticles (Figure 1B) showed that they had spherical morphology with an average size of 126.89 nm. The sizes were uniform and monodisperse. PFpR nanoparticles were synthesized by linking RCQDs to PF through a peptide chain (pep). Energy-dispersive X-ray spectroscopy (EDS) (Figure 1C) indicated the presence of C, N, O, Fe, and S elements, which is demonstrative of the successful assembly of PFpR, and this conclusion is also supported by the TEM results of Figure S2. PFpR was subsequently encapsulated in MG-63 cell membrane to form a "Trojan horse" nanosystem, PFpR@CM. The TEM image (Figure 1D) clearly showed that PFpR was encapsulated in the cell membrane. More relevant material characterization data in Supporting Information (SI, Figures S3 to S7).

***In Vitro* Treatment of PFpR@CM and Effect of Fluorescent Signal Reporting.** Fe-doped PDA nanoparticles can release Fe^{2+} into the tumor microenvironment. Fe^{2+} can then react with intracellular H_2O_2 to activate the Fenton reaction, which generates ROS.[38] To evaluate the efficiency of the Fenton reaction of PF, the generated ROS was detected using methylene blue (MB) as a ROS indicator.[39] The detection was conducted at pH ∼ 6.5 in the presence of H_2O_2. Upon being oxidized by ROS, the blue color of MB faded, and a characteristic absorbance peak at 660 nm was observed. The colorimetric changes of MB under varying PF concentrations are shown in Figure S8. As shown in Figure S9A and B, ROS production increased linearly with PF concentration, which is demonstrative of an efficient Fenton reaction. The time-dependent ROS generation caused by PF (100 μg/mL) is presented in Figure S9C and D. The inset shows a linear comparison between the ROS production caused by PF and that caused by $FeCl_2$ (containing equivalent Fe^{2+} amounts, measured via ICP and o-diazophenol spectrophotometry[40]) under the same conditions. The comparable slopes of the two samples confirm the efficient Fenton reaction caused by PF.

ROS leads to the activation of the pyroptosis pathway by triggering caspase-1 activation.[41] PFpR@CM was used as a fluorescent probe to detect caspase-1, and RCQDs were used as the signal reporter group. The fluorescence of RCQDs was quenched by FRET effect by connecting RCQDs with PDA using peptide chains. When caspase-1 is present, it can split the peptide chain, separating RCQDs from PDA, and the FRET effect is destroyed, leading to fluorescence recovery. Figure S10 shows that the fluorescence of RCQDs was stable under neutral and weakly acidic pH conditions, and the intensity was moderate at pH ∼ 7. Furthermore, Figure S11 demonstrates that the fluorescence of RCQDs was unaffected by common ionic interferences, which suggests that RCQDs can be used as

https://doi.org/10.1021/acs.analchem.5c00107

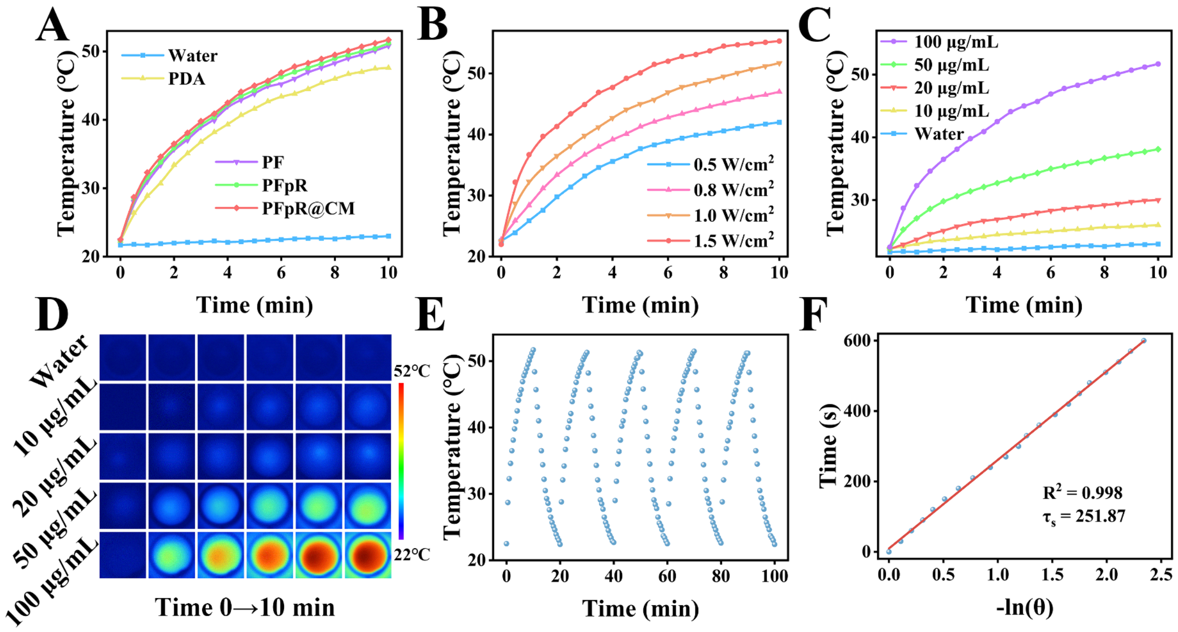

Figure 3. (A) Variations of temperature with time of different materials under NIR laser irradiation. (B) Changes of temperatures with time under NIR laser irradiation at different powers. (C) Temperature profiles of PFpR@CM at different concentrations under NIR laser irradiation. (D) Thermograms of PFpR@CM at different concentrations under NIR laser irradiation. (E) A plot of temperature versus time for PFpR@CM after 5 heating/cooling cycles. (F) Relationship between time and the negative logarithm of temperature drive.

reliable fluorescence signal reporters. The fluorescence of RCQDs remained stable for over 10 days (Figure 2A). PFpR@CM was incubated with 1.0 U/mL caspase-1 in PBS (pH 7.4) at 37 °C, and its response was assessed. Changes in fluorescence intensity over time (Figure 2B) showed that the optimal activation occurred at 30 min. Under an excitation wavelength of 550 nm, PFpR@CM exhibited fluorescence with intensity linearly correlated with caspase-1 concentrations ranging from 0.05 to 1.0 U/mL (Figure 2C, D). The linear regression equation for the correlation was Y = 1102.660X + 572.418, with R^2 = 0.997. The limit of detection (LOD) was 0.024 U/mL (LOD = $3\sigma/k$, where σ is the standard deviation based on 11 blank control samples and k is the slope of the calibration curve). The fluorescence signal was significantly suppressed when a specific caspase-1 inhibitor was added (Figure 2E), which confirms the specificity of PFpR@CM to caspase-1. Anti-interference tests (Figure 2F) indicated that the fluorescence of PFpR@CM remained stable in the presence of common biological interfering substances. These results further validate its suitability for *in vitro* applications.

In addition to its fluorescence-based tumor detection capability, PFpR@CM had excellent photothermal properties, attributed to polydopamine in its structure.[42] Upon 808 nm laser irradiation, PFpR@CM exhibited superior photothermal effects compared to water, PDA, PF, and PFpR, as shown in Figure 3A and Figure S12. The addition of Fe enhanced the photothermal performance of PDA. Figure 3B and Figure S13 illustrate the temperature profiles of PFpR@CM under varying laser power densities, showing that the higher power densities, the greater the increase in temperature. In subsequent experiments, 1.0 W/cm^2 was selected to balance therapeutic efficacy and minimize potential biological damage. The photothermal response of PFpR@CM at different concentrations under 808 nm laser irradiation (1.0 W/cm^2 for 10 min) is shown in Figure 3C and D. As shown, higher PFpR@CM concentrations resulted in a faster temperature increase and higher maximum temperatures. Figure 3E and F depicts the photothermal stability of PFpR@CM, in which consistent heating performance could be observed across five on−off laser cycles, and the maximum temperature was ∼51 °C. Calculated based on the cooling curve, the photothermal conversion efficiency was 24.7%, which confirms that PFpR@CM is a robust and efficient carrier for photothermal therapy.

Intracellular Fluorescence Signaling and Therapeutic Effect of PFpR@CM. Experimental results related to intracellular fluorescent signaling by PFpR@CM and discussion in SI (Figures S14 to S15). To investigate ROS generation, PF and PF@CM (lacking RCQDs, which help to avoid interference) were used. The content of intracellular ROS was measured using the DCFH-DA probe[43] (Figure 4A), and the corresponding fluorescence intensity data are shown in Figure 4B. ROS levels were found to increase with increasing PF and PF@CM concentrations, and the CM modification further enhanced the ROS generation. Pretreatment with vitamin C (an antioxidant) significantly suppressed the fluorescence, confirming that ROS was generated. The results from flow cytometry (Figure 4C) showed consistent trends with those from fluorescence imaging, which is indicative of PF's ability to induce intracellular ROS generation. Calcein-AM/PI staining was performed to observe cell viability. As shown in Figure 4D, prolonged incubation resulted in increased cell death. Comparisons between PF and PDA groups demonstrated that cell death caused by Fe doping was more pronounced, and CM modifications promoted the entry of the nanoparticles and exacerbated the effect. The use of 808 nm photothermal irradiation further enhanced cell death. Scratch and Transwell assays of cells under different treatments (Figure 4E) were analyzed (Figure 4F, G). The results aligned with the calcein-AM/PI staining results, demonstrating that PFpR@CM could effectively inhibit cell migration and invasion, particularly under photothermal irradiation.

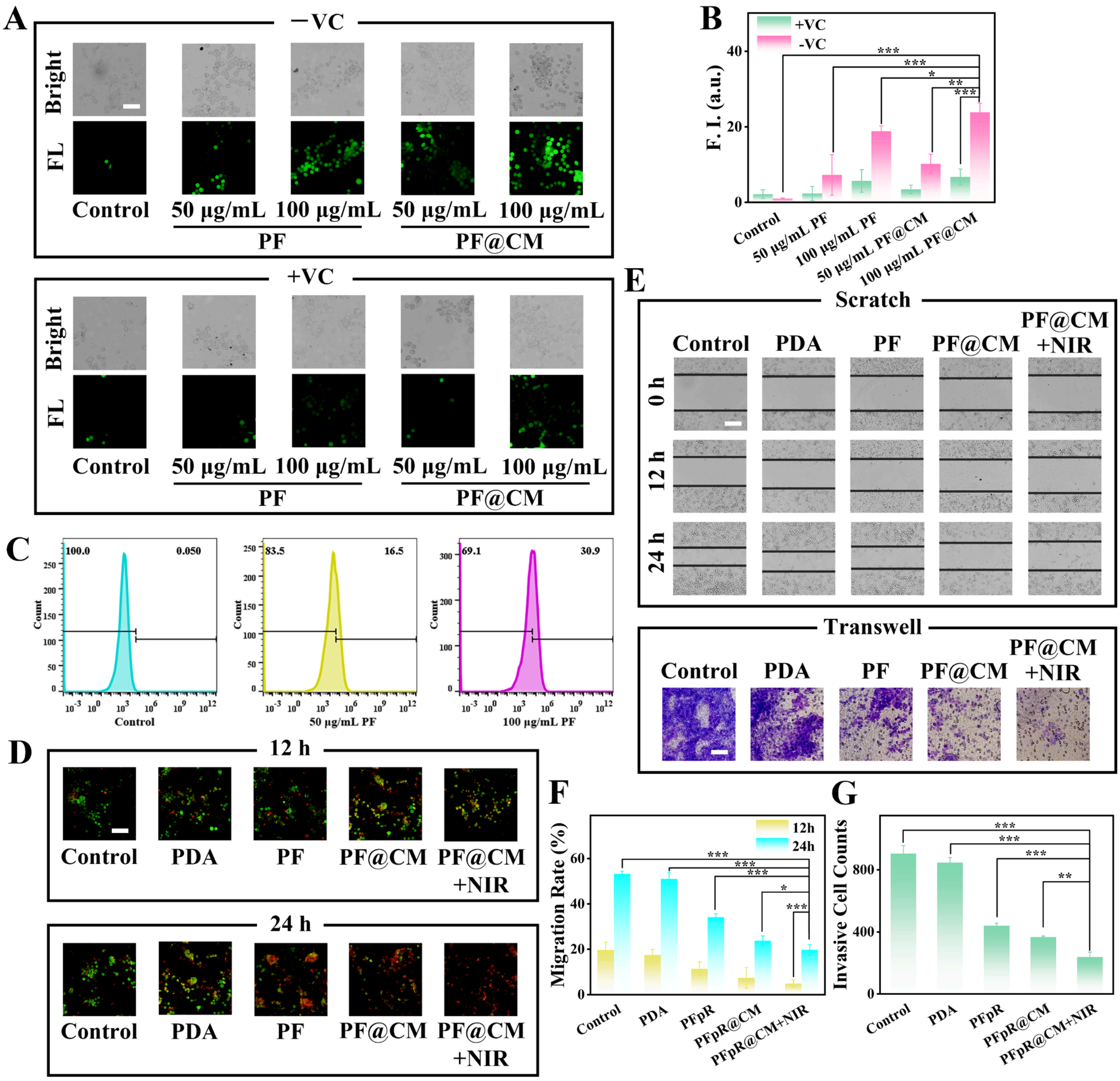

Figure 4. (A) Intracellular ROS generation detected using the ROS fluorescent probe DCFH-DA (scale bar: 80 μm). (B) Fluorescence intensities of cells in (A). (C) Changes in intracellular fluorescence of DCFH-DA were analyzed by flow cytometry. (D) Cell viability assayed by calcein-AM/PI after coincubation of MG-63 cells with PBS, PDA, PF, PF@CM, and PF@CM+NIR (scale bar: 80 μm). (E) Cell scratch and Transwell assays of cells under different conditions (scale bar: 150 μm). (F) Analysis of data in (E) under scratch assay. (G) Analysis of data in (E) under Transwell assay.

These results collectively demonstrate that the "Trojan horse" PFpR@CM has integrated diagnostic and therapeutic functions, including fluorescence signaling, targeted delivery, ROS generation, and photothermal therapy, and thus is suitable for enhanced tumor treatment.

***In Vivo* Therapeutic Efficacy of PFpR@CM.** The biosafety of PFpR@CM was first assessed using a hemolytic assay. The data showed that PFpR@CM had no significant hemolytic effect (Figure S16). To minimize variability, the formulations were intratumorally injected into the tumor site. As shown in Figure 5A, PBS, PpR, PFpR, PFpR+VC, and PFpR+inhibitor were injected into the tumor sites of MG-63 tumor-bearing nude mice. We observed that the fluorescence intensity of mice in all groups increased over time, and the fluorescence of the PFpR+VC and PFpR+inhibitor groups was lower compared to other groups. As shown in Figure 5B, the tumor site intravenously injected with PFpR@CM exhibited strong fluorescence signals. This indicates that PFpR@CM has tumor-targeting capability. In contrast, no significant fluorescence was detected in the PFpR group. Thermal images of tumors in the tail-vein-injection groups (PFpR@CM and PFpR, Figure S17) further confirmed the photothermal properties of PFpR@CM. To evaluate antitumor efficacy, saline, PpR, VC, PFpR, PFpR@CM, PFpR@CM+VC, and PFpR@CM+NIR were administered to MG-63 tumor-bearing nude mice via tail vein injections. Tumor volumes and body weights of the mice were monitored daily for 15 days, after which the mice were dissected and subjected to histopathological analysis (Figure 5C). Tumor photographs and growth curves (Figures 5D, F) revealed that PFpR significantly inhibited tumor growth, and PFpR@CM exhibited even more enhanced inhibitory effects due to CM modifications.

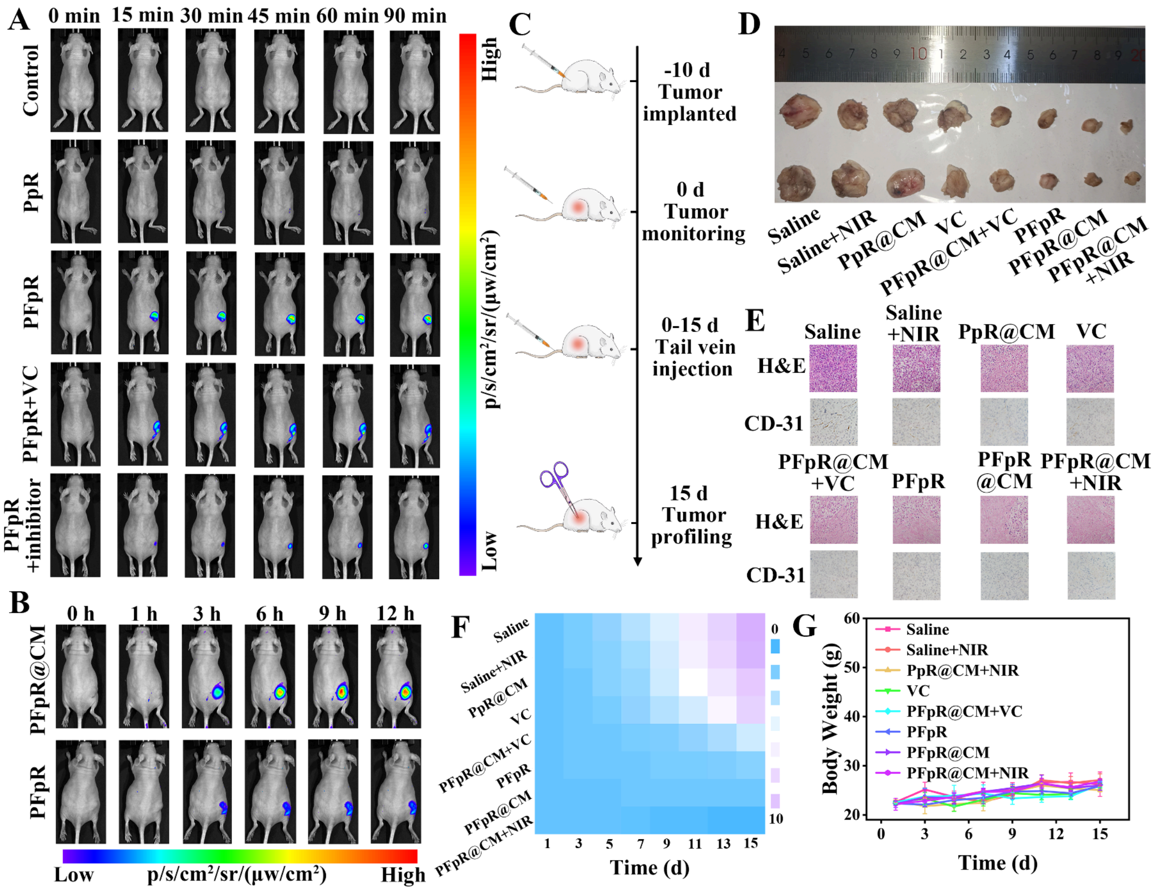

Figure 5. (A) Fluorescence images of MG-63 hormonal mice intratumorally injected with PBS, PpR, PFpR, PFpR+VC, and PFpR+inhibitor. (B) Fluorescence images of MG-63 hormonal mice injected through the tail vein with PFpR and PFpR@CM. (C) Flowchart of *in vivo* experiments. (D) Photographs of tumors dissected from mice in different treatment groups. (E) H&E- and CD-31-stained pathological sections of tumors of mice in different treatment groups (×20 magnification). (F) Mean tumor volumes of mice in different treatment groups. (G) Changes in body weight of mice after different treatments.

The addition of VC reduced the inhibitory effect of PFpR@CM, which is consistent with the known antioxidant properties of VC. VC alone did not significantly exhibit tumor growth. Importantly, the combination of PFpR@CM and NIR photothermal therapy further amplified tumor suppression, demonstrating the synergistic therapeutic effect. The results from histological analysis also supported these findings. H&E staining of tumor sections (Figure 5E) showed an increase in necrotic areas in the PFpR@CM group compared to controls, and the increase was even higher in the PFpR@CM+NIR group. CD31 staining revealed a decrease in expression levels in all treatment groups, indicating the reduction of tumor vascularization and the inhibition of tumor growth. Furthermore, H&E staining of major organs of mice in the PFpR@CM group showed no significant organ damage (Figure S18), which confirms the biosafety of PFpR@CM.[11] The monitoring of body weight over 15 days (Figure 5G) demonstrated the body weights were stable across all groups, which suggests that the administered formulations have no acute toxic side effects. These results collectively validate the excellent therapeutic efficacy, targeting capability, and biosafety of PFpR@CM, particularly when combined with photothermal therapy.

■ CONCLUSION

In conclusion, we successfully designed and synthesized a fluorescence-driven "Trojan horse" nanosystem (PFpR@CM) with integrated tumor-targeting, high-sensitivity Caspase-1 detection, and synergistic ferroptosis-photothermal therapy capabilities. This nanosystem addresses critical limitations of traditional osteosarcoma treatments, such as chemotherapy resistance and delayed therapeutic feedback, by enabling precise tumor localization, real-time ROS monitoring, and enhanced therapeutic efficacy. With a detection limit of 0.024 U/mL and a linear range of 0.05−1.0 U/mL, the system demonstrates exceptional analytical performance for Caspase-1 as a biomarker, bridging the gap between diagnostic sensitivity and therapeutic precision. The multifunctional design of PFpR@CM, including its biomimetic cell membrane camouflage and fluorescence-based feedback mechanism, minimizes systemic toxicity while providing real-time insights into tumor microenvironment dynamics. By addressing the limitations of current TME monitoring tools, our work advances the field of analytical chemistry and offers an innovative solution for precision oncology. This nanosystem not only establishes a versatile platform for studying the dynamic interactions within the TME during treatment but also holds significant potential for broader clinical applications in the diagnosis and therapy of complex malignancies such as osteosarcoma.

■ ASSOCIATED CONTENT

Supporting Information

The Supporting Information is available free of charge at https://pubs.acs.org/doi/10.1021/acs.analchem.5c00107.

Additional experimental details, including materials and reagents, instruments, material characterization, *in vitro* Fenton reaction of PF, fluorescence detection of caspase-1 *in vitro* by PFpR@CM, photothermal conversion performance test of PFpR@CM, cell counting kit-8 (CCK-8) assay, *in vitro* cell experiments, *in vivo* experiments and supplementary figures, table, and references (PDF)

■ AUTHOR INFORMATION

Corresponding Authors

Pinyi Ma − *College of Chemistry, Jilin Province Research Center for Engineering and Technology of Spectral Analytical Instruments, Jilin University, Changchun 130012, China;* orcid.org/0000-0002-3230-4928; Email: mapinyi@jlu.edu.cn

Shan Jiao − *Hospital of Stomatology, Jilin University, Changchun 130021, China*; Email: jiaoshan@jlu.edu.cn

Daqian Song − *College of Chemistry, Jilin Province Research Center for Engineering and Technology of Spectral Analytical Instruments, Jilin University, Changchun 130012, China;* orcid.org/0000-0002-4866-1292; Email: songdq@jlu.edu.cn

Authors

Chen Zhao − *College of Chemistry, Jilin Province Research Center for Engineering and Technology of Spectral Analytical Instruments, Jilin University, Changchun 130012, China*

Mo Ma − *College of Chemistry, Jilin Province Research Center for Engineering and Technology of Spectral Analytical Instruments, Jilin University, Changchun 130012, China; School of Pharmacy, Jilin University, Changchun 130012, China*

Jukun Yang − *College of Chemistry, Jilin Province Research Center for Engineering and Technology of Spectral Analytical Instruments, Jilin University, Changchun 130012, China*

Jingdan Sun − *Department of Chemistry, University of Washington, Seattle, Washington 98195, United States*

Ying Sun − *College of Chemistry, Jilin Province Research Center for Engineering and Technology of Spectral Analytical Instruments, Jilin University, Changchun 130012, China;* orcid.org/0000-0002-6820-3184

Complete contact information is available at: https://pubs.acs.org/10.1021/acs.analchem.5c00107

Notes

The authors declare no competing financial interest.

■ ACKNOWLEDGMENTS

This work was supported by the National Key R&D Program of China (No. 2021YFF0600701), the National Natural Science Foundation of China (22074052 and 22004046), and the Science and Technology Developing Foundation of Jilin Province of China (20230101033JC).

■ REFERENCES

(1) Kundu, M.; Butti, R.; Panda, V. K.; Malhotra, D.; Das, S.; Mitra, T.; Kapse, P.; Gosavi, S. W.; Kundu, G. C. *Mol. Cancer* **2024**, *23*, 92.

(2) Ma, K.; Wang, L.; Li, W.; Tang, T.; Ma, B.; Zhang, L.; Zhang, L. *Trends Cancer* **2025**, *11*, 18.

(3) Zhao, Y.; Shen, M.; Wu, L.; Yang, H.; Yao, Y.; Yang, Q.; Du, J.; Liu, L.; Li, Y.; Bai, Y. *Cell Death Dis.* **2023**, *14*, 587.

(4) Knipper, K.; Lyu, S. I.; Quaas, A.; Bruns, C. J.; Schmidt, T. *Int. J. Mol. Sci.* **2023**, *24*, 13482.

(5) Grasso, G.; Colella, F.; Forciniti, S.; Onesto, V.; Iuele, H.; Siciliano, A. C.; Carnevali, F.; Chandra, A.; Gigli, G.; Del Mercato, L. L. *Nanoscale Adv.* **2023**, *5*, 4311−4336.

(6) Prasad, P.; Gordijo, C. R.; Abbasi, A. Z.; Maeda, A.; Ip, A.; Rauth, A. M.; DaCosta, R. S.; Wu, X. Y. *ACS Nano* **2014**, *8*, 3202−3212.

(7) Meng, X.; Wu, Y.; Bu, W. *Adv. Healthc. Mater.* **2021**, *10*, No. e2000912.

(8) Hu, Q.; Huang, Z.; Duan, Y.; Fu, Z.; Liu, B. *Bioconjug Chem.* **2020**, *31*, 1268−1278.

(9) Balcioglu, H. E.; Wijers, R.; Smid, M.; Hammerl, D.; Trapman-Jansen, A. M.; Oostvogels, A.; Timmermans, M.; Martens, J. W. M.; Debets, R. *npj Imaging* **2024**, *2*, 21.

(10) Zhao, C.; Ma, M.; Yang, J.; Liu, L.; Ma, P.; Wu, Q.; Song, D. *Chem. Eng. J.* **2024**, *497*, 154462.

(11) Liu, L.; Li, X.; Zhang, H.; Chen, H.; Abualrejal, M. M. A.; Song, D.; Wang, Z. *Sens. Actuators B Chem.* **2021**, *333*, 129554.

(12) Duan, Q. J.; Zhao, Z. Y.; Zhang, Y. J.; Fu, L.; Yuan, Y. Y.; Du, J. Z.; Wang, J. *Adv. Drug Delivery Rev.* **2023**, *196*, 114793.

(13) Clerc, P.; Jeanjean, P.; Hallali, N.; Gougeon, M.; Pipy, B.; Carrey, J.; Fourmy, D.; Gigoux, V. *J. Controlled Release* **2018**, *270*, 120−134.

(14) Wang, Z.; Li, H.; Zhou, W.; Lee, J.; Liu, Z.; An, Z.; Xu, D.; Mo, H.; Hu, L.; Zhou, X. *Biomaterials* **2022**, *290*, 121842.

(15) Zhang, Y.; Zhang, K.; Yang, H.; Hao, Y.; Zhang, J.; Zhao, W.; Zhang, S.; Ma, S.; Mao, C. *ACS Appl. Mater. Interfaces* **2023**, 14099−14110.

(16) Li, Y.; Qian, L.; Yang, Z.; Li, S.; Wu, A.; Wang, X. *Colloids Surf. B Biointerfaces* **2024**, *239*, 113911.

(17) Deng, H.; Zhang, J.; Yang, Y.; Yang, J.; Wei, Y.; Ma, S.; Shen, Q. *ACS Appl. Mater. Interfaces* **2022**, *14*, 24089−24101.

(18) Li, A.; Zhao, J.; Fu, J.; Cai, J.; Zhang, P. *Asian J. Pharm. Sci.*. **2021**, *16*, 161−174.

(19) Feng, Y.; Liao, Z.; Zhang, H.; Xie, X.; You, F.; Liao, X.; Wu, C.; Zhang, W.; Yang, H.; Liu, Y. *Chem. Eng. J.* **2023**, *452*, 139506.

(20) Myung, J. H.; Park, S. J.; Wang, A. Z.; Hong, S. *Adv. Drug Delivery Rev.* **2018**, *125*, 36−47.

(21) Wang, G.-G.; Lv, Q.-Y.; Song, X.; Cui, H.-F. *Sens. Actuators B Chem.* **2021**, *344*, 130285.

(22) Wang, H.; Yang, S.; Chen, L.; Li, Y.; He, P.; Wang, G.; Dong, H.; Ma, P.; Ding, G. *Bioact. Mater.* **2024**, *33*, 174−222.

(23) Wang, F.; Dong, X.; Zuo, Y.; Xie, Z.; Guan, R. *Mater. Today Phys.* **2024**, *41*, 101332.

(24) Wang, Q.; Zhang, T.; Cheng, Q.; Wang, B.; Liu, Y.; Xing, G.; Tang, Z.; Qu, S. *Adv. Funct. Mater.* **2024**, *34*, 2402976.

(25) Madonia, A.; Minervini, G.; Terracina, A.; Pramanik, A.; Martorana, V.; Sciortino, A.; Carbonaro, C. M.; Olla, C.; Sibillano, T.; Giannini, C.; Fanizza, E.; Curri, M. L.; Panniello, A.; Messina, F.; Striccoli, M. *ACS Nano* **2023**, *17*, 21274−21286.

(26) Bian, X.; Fan, N.; Li, M.; Han, D.; Li, J.; Fan, L.; Li, X.; Kong, L.; Tang, H.; Ding, S.; Song, F.; Li, S.; Cheng, W. *ACS Nano* **2023**, *17*, 4896−4912.

(27) Chen, J.; Duan, Z.; Deng, L.; Li, L.; Li, Q.; Qu, J.; Li, X.; Liu, R. *Adv. Healthc. Mater.* **2024**, *13*, No. e2304436.

(28) Luo, T.; Fan, Z.; Zeng, A.; Wang, A.; Pan, Y.; Xu, Y.; Chen, H.; Chen, W.; Nie, D.; Lin, J.; Huang, A.; Gong, M.; Huang, Y.; Ding, Y.; Zhu, X.; Rao, L.; Wang, J. *Adv. Sci.* **2025**, *12*, 2410427.

(29) Zhao, C.; Ma, M.; Yang, J.; Ye, Z.; Ma, P.; Song, D. *Anal. Chem.* **2024**, *96*, 16053−16062.

(30) Tang, L.; Mo, S.; Liu, S. G.; Liao, L. L.; Li, N. B.; Luo, H. Q. *Sens. Actuators B Chem.* **2018**, *255*, 754−762.

(31) Li, Y.; Ke, J.; Jia, H.; Ren, J.; Wang, L.; Zhang, Z.; Wang, C. *Colloids Surf. B Biointerfaces* **2023**, *222*, 113131.

(32) Zeng, F.; Tang, L.; Zhang, Q.; Shi, C.; Huang, Z.; Nijiati, S.; Chen, X.; Zhou, Z. *Angew. Chem., Int. Ed. Engl.* **2022**, *61*, No. e202112925.

(33) Li, H.; Su, D.; Gao, H.; Yan, X.; Kong, D.; Jin, R.; Liu, X.; Wang, C.; Lu, G. *Anal. Chem.* **2020**, *92*, 3198−3205.

(34) Zhu, Y.; Xin, N.; Qiao, Z.; Chen, S.; Zeng, L.; Zhang, Y.; Wei, D.; Sun, J.; Fan, H. *ACS Appl. Mater. Interfaces* **2019**, *11*, 43018−43030.

(35) Song, S.; Zhang, Y. *J. Mater. Chem. A* **2017**, *5*, 22352−22360.

(36) Chen, K.; Chen, X.; Hu, K.; Zhao, Y.; Liu, Y.; Liu, G.; Chen, J.; Jiang, W.; Shuai, Z.; Qu, D.-H.; Wang, Z. *Sci. China Chem.* **2024**, *67*, 1324−1333.

(37) Liu, S. H.; Cui, H.; Huang, J. B.; Tian, B. S.; Bao, J. C. *Mater. Lett.* **2024**, *377*, 137347.

(38) Zhang, K.; Wu, J.; Zhao, X.; Qin, J.; Xue, Y.; Zheng, W.; Wang, L.; Wang, H.; Shen, H.; Niu, T.; Luo, Y.; Tang, R.; Wang, B. *ACS Nano* **2021**, *15*, 19838−19852.

(39) Chen, X.; Yang, S.; Shao, H.; Wang, S.; Xie, J.; Liu, Q.; Huang, Y.; Gan, N.; Huang, S. *Chem. Eng. J.* **2024**, *498*, 155897.

(40) Yang, L.; Yao, G. *Int. J. Environ. Anal. Chem.* **2022**, *102*, 3194−3206.

(41) Xu, Z.; Shen, J.; Lin, L.; Chen, J.; Wang, L.; Deng, X.; Wu, X.; Lin, Z.; Zhang, Y.; Yu, R.; Xu, Z.; Zhang, J.; Zhang, Y.; Wang, C. *Environ. Int.* **2023**, *181*, 108296.

(42) Ding, F.; Gao, X.; Huang, X.; Ge, H.; Xie, M.; Qian, J.; Song, J.; Li, Y.; Zhu, X.; Zhang, C. *Biomaterials* **2020**, *245*, 119976.

(43) Yu, D.; Zha, Y.; Zhong, Z.; Ruan, Y.; Li, Z.; Sun, L.; Hou, S. *Sens. Actuators B Chem.* **2021**, *339*, 129878.